Small

NANO · MICRO small
www.small-journal.com

RESEARCH ARTICLE OPEN ACCESS

High-Rate and Selective Conversion of Low-Concentration Carbon Dioxide to Carbon Monoxide Using a Carbon Nanotube-Supported Molecular Electrocatalyst

Tzu-Hsuan Wang[1] | Fitri Nur Indah Sari[1] | Yen-Peng Cheng[1] | Eunice Estrella De Guzman[1] | Adriana Matamoros-Veloza[2] | Miller Alonso Camargo-Valero[3,4] | Chia-Yu Lin[1,5,6]

[1]Department of Chemical Engineering, National Cheng Kung University, Tainan, Taiwan | [2]School of Chemistry, University of Leeds, Leeds, UK | [3]BioResource Systems Research Group, School of Civil Engineering, University of Leeds, Leeds, UK | [4]Department of Civil Engineering and Planning, Faculty of Engineering, Universitas Negeri Malang, Malang, Indonesia | [5]Center for Resilience and Intelligence on Sustainable Energy Research (RiSER), National Cheng Kung University, Tainan, Taiwan | [6]Program On Key Materials & Program on Smart and Sustainable Manufacturing Academy of Innovative Semiconductor and Sustainable Manufacturing, National Cheng Kung University, Tainan, Taiwan

Correspondence: Miller Alonso Camargo-Valero (M.A.Camargo-Valero@leeds.ac.uk) | Chia-Yu Lin (cyl44@mail.ncku.edu.tw)

Received: 6 October 2025 | **Revised:** 23 December 2025 | **Accepted:** 23 January 2026

Keywords: biogas upgrading | CO_2 affinity | carbon mitigation | diluted CO_2 | electrochemical upcycling of CO_2 | metal phthalocyanine

ABSTRACT

Electrocatalytic CO_2 reduction reaction (e-CO_2RR), powered by renewable electricity, is a compelling strategy to valorize CO_2 into valuable chemicals and fuels. Herein, we report on MWCNT|CuPc-CoPc-modified gas-diffusion electrodes (GDEs) featuring molecular-level dispersion of cobalt phthalocyanine (CoPc) and copper phthalocyanine (CuPc) on the multi-walled carbon nanotube (MWCNT) support. The introduction of CuPc effectively mitigates CoPc aggregation, enabling tunable loading and fractional accessibility of electrochemically active CoPc sites, alongside improved CO_2 adsorption capacity. Besides, the synergistic electronic interactions among CoPc, MWCNT, CuPc, and H_2Pc, formed in situ via CuPc demetallization during electrolysis, optimized CO_2 affinity, as evidenced by density functional theory calculations. With these promising attributes, the MWCNT|CuPc-CoPc-modified GDE with optimized CuPc content exhibits promising e-CO_2RR performance across a wide CO_2 concentration range (20%–98%). Notably, an efficient single-pass conversion of CO_2 to CO is achieved, yielding a high CO yield of 65.7 ± 2.3% and an energy efficiency of 54.8 ± 1.9% using 20% CO_2 at an ampere-level current (0.625 A). Furthermore, the developed electrode demonstrated robust stability, maintaining FE_{CO} above 80.4% over 72-h electrolysis under a simulated biogas atmosphere (40% CO_2/60% CH_4). These findings underscore the strong promise of molecularly engineered catalyst systems for efficient and selective CO production from low-concentration CO_2 emission sources.

1 | Introduction

Electrochemical CO_2 reduction (e-CO_2RR) under ambient conditions, driven by green electricity, offers a sustainable pathway for resourcing CO_2 into commodity chemicals and high-energy fuels, contributing to carbon mitigation, green chemical synthesis, and renewable energy storage [1, 2]. However, the inherent chemical inertness of CO_2 molecules and the complexity of the multi-step proton-coupled electron transfer processes involved in e-CO_2RR often lead to sluggish reaction kinetics and diverse competing side reactions, posing significant challenges for achieving high product selectivity. Moreover, given that the CO_2 content in most emission sources is less than 45%, and the enrichment of CO_2 streams via carbon capture is both energy- and

cost-intensive, the direct utilization of low-concentration CO_2 holds a transformative impact on decarbonization efforts. Despite this, most studies on *e*-CO_2RR have focused on the performance characterization of developed electrocatalysts under highly pure CO_2 atmospheres, while investigations under dilute CO_2 conditions remained limited [3–11]. Electrochemical reduction of low-concentration CO_2 directly at emission sites often suffers from low Faradaic efficiency and poor product selectivity due to the mass-transfer limitation and the presence of impurity gases [3–7]. To render *e*-CO_2RR economically viable, the development of robust and efficient electrocatalysts capable of selectively converting low-concentration CO_2 directly from emission sources into targeted products with minimal energy input is therefore imperative.

Among the products generated via *e*-CO_2RR, carbon monoxide (CO) has received particular interest due to its broad utility in the medical, chemical, and metallurgical industries [12]. To date, several electrocatalysts have been developed for the selective CO production via *e*-CO_2RR at low overpotentials ($\eta < -0.5$ V) [13–18]. Among them, molecular complexes, such as cobalt phthalocyanine (CoPc) and cobalt tetraphenylporphyrin, have received great attention due to their ability to convert CO_2 into CO with high selectivity at a low overpotential, their molecular size providing extremely high active sites per geometric surface area, and a clear and controllable structure-property relationship, which is beneficial for subsequent performance optimization [19–23]. However, their strong π–π stacking interactions among the MPc molecules often lead to aggregation in solution or upon deposition on the electrode surface, especially at high MPc concentrations. This aggregation severely compromises overall catalytic performance by reducing the accessible active sites and diminishing electronic conductivity [24–26]. For example, the turnover frequency for CO production (TOF_{CO}) decreased from ~100 to ~7 s^{-1} at −0.73 V vs. RHE when the loading amount of CoPc was increased from 2×10^{-11} mol cm^{-2} to 1×10^{-9} mol cm^{-2} [27]. In addition, the CoPc decomposed under highly cathodic potentials due to the undesirable reduction of the phthalocyanine ligands, further deteriorating the activity of CoPc at industrially relevant operation current densities [27, 28]. To address these issues, several strategies have been developed, including the utilisation of porous carbon supports [19, 26, 29, 30] and ligand functionalization of MPcs [25, 27, 31–33]. For instance, Wang and his coworkers reported that the detrimental reduction of the phthalocyanine ligand can be suppressed by appending electron-donating amino substituents to the phthalocyanine ring to enhance the metal–ligand bond strength [27]. Zhu et al. reported host–guest interaction between tetra-crown ether substituted CoPc and K^+ ions, which not only eliminated catalyst aggregation but also strengthened catalyst-support interactions, achieving a high TOF_{CO} of 111 s^{-1} and high current density of 38 mA cm^{-2} at the expense of a moderate η of −0.57 V [31]. Recently, Wang et al. synthesized an ultrathin conjugated microporous polymer sheath around carbon nanotubes by an ionothermal copolymerization of CoPc and H_2Pc using the Scholl reaction. With the synergistic effect of H_2Pc moieties as proton/electron donors, the resultant composites selectively generated CO with a high TOF_{CO} of 27.1 s^{-1} at −0.65 V vs. RHE [34]. Very recently, He et al. reported that the inclusion of sulfylphenoxy group and cross-linking with polypyrrole significantly enhanced the CO_2 affinity of CoPc, thereby resulting in a high Faradaic efficiency (FE_{CO}: ~95.6%) and an acceptable TOF_{CO} (0.34 s^{-1}) towards CO production from the conversion of 48% CO_2 at the expense of a moderate η of −0.79 V [35]. Beyond the challenge of molecular aggregation, the *e*-CO_2RR into CO over CoPc is typically limited by the initial activation step ($* + e^- + CO_2 \rightarrow {}^*CO_2^-$) [36], a process that remains relatively understudied. The incorporation of Cu into Co-containing catalysts has been demonstrated to be crucial in modulating the charge distribution surrounding the Co center, thereby tuning the affinity of the Co metal center toward the reaction intermediates [37]. Despite these advances, the applications of CoPc for the conversion of low-concentration CO_2 at industrially relevant current densities (>100 mA cm^{-2}) remain largely unexplored.

In the present contribution, we report a facile H_2SO_4-assisted impregnation method for the preparation of MWCNT|CuPc-CoPc-modified gas-diffusion electrodes (GDEs) featuring molecular-level dispersion of CoPc and copper phthalocyanine (CuPc) on the multi-walled carbon nanotube (MWCNT) support. Incorporating CuPc during the electrode preparation effectively mitigated CoPc aggregation, enabling tunable loading and fractional accessibility (θ) of electrochemically active CoPc sites. In particular, the MWCNT|CuPc-CoPc-modified GDE, prepared with optimized CuPc content, exhibited a significantly-enhanced θ of 0.32, attributed to the in situ CuPc demetallization during electrolysis, which facilitated the exposure of previously buried CoPc active sites. Furthermore, the synergistic electronic interactions among CoPc, MWCNT, CuPc, and H_2Pc, formed in situ via CuPc demetallization during electrolysis, optimized CO_2 affinity, as evidenced by density functional theory calculations. With significantly enhanced accessibility, optimized CO_2 affinity, and CO_2 adsorption capacity of CoPc active sites, the MWCNT|CuPc-CoPc-modified GDE, prepared with optimized CuPc content, exhibited promising *e*-CO_2RR performance across a wide range of CO_2 concentrations (20%–98%). Notably, this work marks the first demonstration of a high CO yield of 65.7 ± 2.3% and a high energy efficiency of 54.8 ± 1.9% from single-pass conversion of 20% CO_2 at an ampere-level current (0.625 A) using a molecular catalyst-based modified electrode. Moreover, the electrode also exhibited promising stability, maintaining a FE_{CO} above 80.4% over 72-h electrolysis under simulated biogas atmosphere (40% CO_2 and 60% CH_4). These results highlight the strong potential of the developed molecularly-engineered catalyst system for efficient and selective CO production from the conversion of low-concentration CO_2 directly from emission sources, with relevance to scalable carbon utilization technologies.

2 | Results and Discussion

2.1 | Materials Synthesis and Characterizations

As revealed in Figure S1 and the discussion in Dispersity of CoPc in Supporting Information, CoPc exhibited pronounced aggregation and precipitation in N, N-dimethylformamide (DMF), but it remained molecularly dispersed in concentrated H_2SO_4 at high CoPc concentration (~0.9 mM) with no visible precipitation of CoPc after static incubation for several hours. The highly dispersed CoPc in concentrated H_2SO_4 is attributed to the protonation of CoPc in H_2SO_4 into $[CoPcH]^+$ [38, 39], which

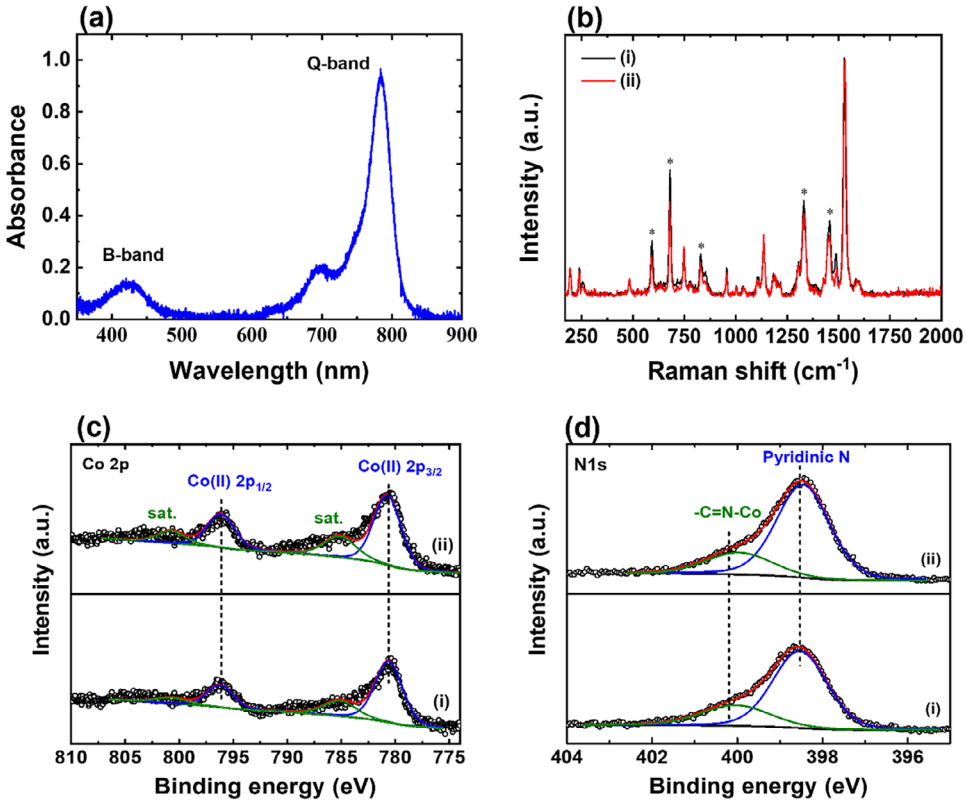

FIGURE 1 | (a) UV–vis spectrum of CoPc-containing concentrated H_2SO_4 after 4-h static standing. (b) Raman spectra, and (c,d) XPS spectra of (i) the pristine CoPc powder and (ii) CoPc powder recovered from the H_2SO_4 dispersion. (c) Co 2p region and (d) N 1s region.

induces electrostatic repulsion and enhances dispersibility. The UV–vis spectrum of the CoPc-containing H_2SO_4 solution, shown in Figure 1a, exhibited two typical absorption peaks of the Pc molecule, which are the Soret or B-band at the wavelength of 430 nm and the Q-band at the wavelength of 790 nm [40, 41]. These bands originate from $\pi \rightarrow \pi^*$ transition between bonding and antibonding molecular orbitals [42]. The Q-band serves as an indicator of molecular aggregation; its strong and well-defined absorption indicates that CoPc was molecularly dispersed without aggregation [24, 43, 44]. In addition, the presence of both B-band and Q-band confirms that the CoPc structure remained intact in concentrated H_2SO_4. Raman analyses (Figure 1b) showed that CoPc powder recovered from the H_2SO_4 dispersion retained spectra features consistent with pristine CoPc powder, indicating structural preservation. Similarly, XPS analyses (Figure 1c,d) revealed that the recovered CoPc powder exhibited the same XPS features to that of pristine CoPc powder, including (i) two distinct peaks at 780.7 and 796.4 eV in the Co 2p region, corresponding to Co(II) $2p_{3/2}$ and Co(II) $2p_{1/2}$, respectively [45], and (ii) two peaks at 398.4 and 400.1 eV in the N 1s region, attributed to pyridinic nitrogen and —C═N—Co group, respectively [26, 45]. Collectively, the UV–vis, Raman, and XPS results confirm that CoPc maintained its chemical integrity during dispersion, demonstrating its high chemical stability in concentrated H_2SO_4.

To investigate the correlation between CoPc dispersibility and its *e*-CO_2RR activity, CoPc-SA and CoPc-DMF electrodes were prepared by incubating carbon paper in CoPc (0.2 mg mL^{-1})-containing H_2SO_4 solution and CoPc (0.2 mg mL^{-1})-containing DMF solution under stirring at 200 rpm for 2 h, respectively, and subjected to electrochemical characterizations. The ICP-OES analyses reveal that the CoPc-SA and CoPc-DMF electrodes contained about 14 and 97 nmol cm^{-2} CoPc, respectively. The analysis of linear sweep voltammetry (LSV) (Figure S2) reveals that both CoPc-SA and CoPc-DMF electrodes exhibited enhanced current response upon exposure to CO_2. For example, the current responses of CoPc-SA and CoPc-DMF electrodes at the applied potential of −0.7 V vs. RHE were 2.05 and 1.19 mA cm^{-2} under CO_2 atmosphere (98%), respectively, which were about 2.6 and 1.4 times higher than those obtained under Ar atmosphere. To further confirm that the enhanced current responses resulted from *e*-CO_2RR, additional 2-h controlled-potential electrolysis experiments at −0.7 V vs. RHE were performed in the two-compartment H-cell, and the results are shown in Figure S3. As revealed, the CoPc-SA electrode exhibited a similar Faradaic efficiency (FE_{CO}: 93.9 ± 2.2% vs. 91.6 ± 3.9%) for CO production to the CoPc-DMF electrode. However, the CoPc-SA electrode exhibited significantly higher activity, in terms of CO production rate (R_{CO}: 35.4 ± 1.6 μmol cm^{-2} h^{-1} vs. 18.1 ± 1.2 μmol cm^{-2} h^{-1}) and turnover frequency (TOF_{CO}: 0.70 ± 0.03 s^{-1} *vs.* 0.05 ± 0.00 s^{-1}), than the CoPc-DMF electrode. These findings align with previous reports indicating that the molecularly dispersed CoPc exhibits superior *e*-CO_2RR activity than its aggregated form [25], underscoring the critical role of solvent-dependent dispersibility in determining surface distribution and intrinsic catalytic performance of the deposited CoPc.

Encouraged by the promising *e*-CO_2RR activity of the CoPc-SA electrode, further performance enhancement was explored

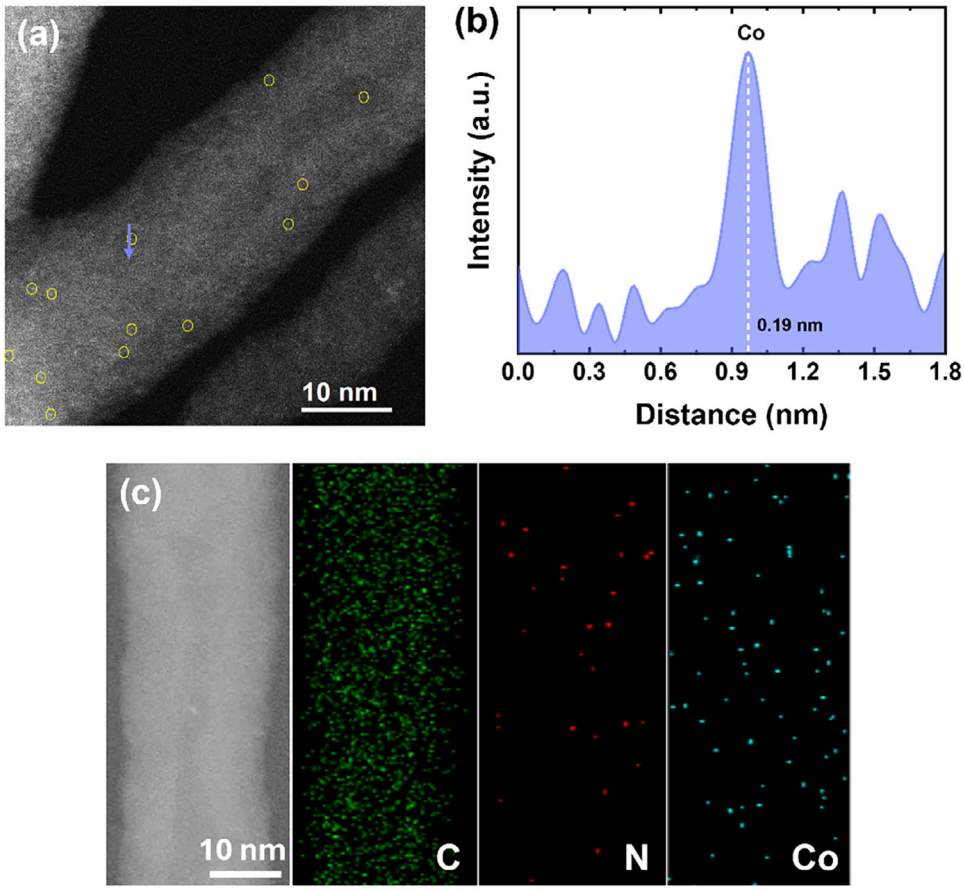

FIGURE 2 | (a) HAADF-STEM image, (b) line profile along the blue arrow in (a), and (c) STEM-EDS elemental mapping of MWCNT|CoPc.

by immobilizing CoPc onto multi-walled carbon nanotubes (MWCNT) and subsequent preparation of the MWCNT-supported CoPc electrode (i.e., MWCNT|CoPc; see Experimental Section for details). The SEM analyses, shown in Figure S4, reveal that the pristine CoPc powder consists of aggregates of CoPc microrods. Nevertheless, after the dispersion in concentrated H_2SO_4 and subsequent immobilization onto the MWCNTs, the obtained MWCNT|CoPc sample exhibited a surface morphology resembling that of MWCNTs, with no observable aggregation of CoPc molecules. Figure S5 shows the XPS spectra of the pristine CoPc powder and MWCNT|CoPc. As revealed, the Co $2p_{1/2}$ and Co $2p_{3/2}$ peaks of MWCNT|CoPc shifted to a higher binding energy compared to the pristine CoPc powder, which implies the oxidation state of Co sites in the MWCNT|CoPc is lower than that in the pristine CoPc powder. This finding indicates a strong interaction between CoPc and MWCNT with the electron transfer from the MWCNT to the Co center [46, 47]. The molecular dispersion of CoPc on MWCNT support was further investigated using high-angle annular dark-field scanning transmission electron microscopy (HAADF-STEM). As shown in Figure 2a, the HAADF-STEM image revealed a high density of isolated bright dots (highlighted by yellow circles) attributed to Co atoms due to their higher Z-contrast relative to carbon atoms, confirming molecular-level dispersion of CoPc on the surface of MWCNT support. The dispersion of isolated Co atoms was further verified by the profiles along the blue arrow in the HAADF-STEM image (Figure 2a). The different atomic intensities can be clearly distinguished, and the highest peak intensity has an atomic radius of the Co atom (0.19 nm), confirming the existence of atomically dispersed Co sites (Figure 2b). The scanning transmission electron microscopy energy-dispersive X-ray spectroscopy (STEM-EDS) analysis reveals the uniform distribution of C, N, and Co elements (Figure 2c). These findings confirm the successful preparation of MWCNT-supported CoPc (*i.e.*, MWCNT|CoPc) featuring molecularly dispersed CoPc species.

Figure 3 shows the temperature-programmed desorption-coupled mass spectrometry (TPD-MS) of the MWCNTs, pristine CoPc powder, and MWCNT|CoPc. While MWCNTs and CoPc powder exhibited negligible CO_2 desorption signal, MWCNT|CoPc showed two distinct desorption peaks at 105°C and 224°C, originating from physically adsorbed CO_2, [48] and had a total CO_2 adsorption capacity of 73.0 μmol CO_2 g^{-1}. The enhanced CO_2 affinity of the MWCNT|CoPc compared to the pristine CoPc powder could be attributed to the significantly higher exposed surface area for CO_2 adsorption sites provided by the molecularly dispersed CoPc molecules and/or the enriched electron density of the cobalt center of CoPc via the strong interaction between CoPc and MWCNT, with the electron transfer from the MWCNT to the Co center (Figure S5) [46, 48].

Figure 4 shows the electrochemical characterization of the *e*-CO_2RR performance of the MWCNT|CoPc electrode under different applied potentials in the two-compartment H-cell. As revealed, the MWCNT|CoPc electrode generated CO with a

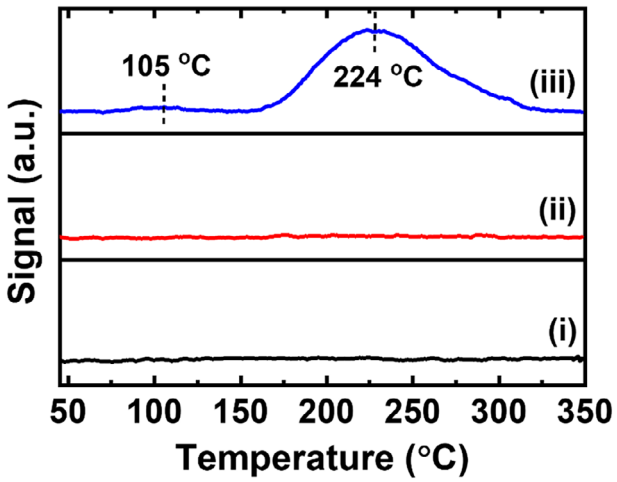

FIGURE 3 | CO_2-TPD profiles of the (i) MWCNTs, (ii) pristine CoPc powder, and (iii) MWCNT|CoPc.

FE_{CO} ≥90% at potentials ranging from −0.55 V vs. RHE to −0.7 V vs. RHE. In addition, both the R_{CO} and TOF_{CO} increased with increasing cathodic potential, reaching maximal values of 216.9 ± 4.2 μmol cm^{-2} h^{-1} and 3.6 ± 0.1 s^{-1}, respectively, at −0.7 V vs. RHE. The generation of methanol (MeOH) onset at −0.8 V vs. RHE with a FE_{MeOH} of 10.1 ± 1.7% at the expense of FE_{CO}, R_{CO}, and TOF_{CO}, which is in agreement with previous reports indicating that MeOH generation via *e*-CO_2RR to MeOH proceeds through a domino pathway, wherein CO_2 is first reduced to CO via a two-electron transfer process, followed by further reduction of CO to MeOH through a four-electron–four-proton transfer process [27]. It is important to note that the MWCNT|CoPc electrode exhibited remarkably higher activity, in terms of R_{CO} (216.9 ± 4.2 vs. 35.4 ± 1.6 μmol cm^{-2} h^{-1}) and TOF_{CO} (3.57 ± 0.07 s^{-1} vs. 0.70 ± 0.03 s^{-1}), than the CoPc-SA electrode at −0.7 V vs. RHE. The enhanced *e*-CO_2RR performance of the MWCNT|CoPc electrode could be attributed to the interaction between CoPc and MWCNT support with the electron transfer from the MWCNT to the Co center, which enriches the electron density of the Co active site, thereby facilitating CO_2 adsorption and activation [34, 46, 48, 54].

2.2 | *e*-CO_2RR Performance With a Gas-Fed Flow Electrolyzer

To mitigate the mass transport limitations inherent to batch-mode operation with H cells, a flow-type electrolyzer was established (Scheme S1, see Experimental Section for details). Furthermore, to achieve high *e*-CO_2RR performance at the industrially relevant applied current densities, MWCNTs-supported CoPc and CuPc with various nominal CuPc/CoPc weight ratios (r), designated as MWCNT|CuPc-CoPc (r) for simplicity, were prepared, and their *e*-CO_2RR performance was systematically investigated. The chemical composition and chemical properties of the prepared electrodes are summarised in Table S1.

Figure 5 and Figures S6 andS7 show the electrochemical characterization of the *e*-CO_2RR performance of the MWCNT|CuPc-CoPc (r)-modified GDE obtained from 2-h electrolysis at −100 mA cm^{-2}. As revealed from Figure S6, the MWCNT|CuPc-modified GDE exhibited negligible *e*-CO_2RR activity, with no detectable CO generation at −100 mA cm^{-2}. The ex situ XPS analysis (Figure S8) confirms that the as-prepared MWCNT|CuPc-modified GDE showed spectral features characteristic of CuPc, including (i) Cu(II) $2p_{3/2}$ and Cu(II) $2p_{1/2}$ peaks at binding energies of 935.2 and 954.9 eV [49], (ii) a pyridinic-N peak at binding energy of 398.6 eV [49], and (iii) a —C═N—Cu peak at binding energy of 400.2 eV [50]. After 2-h electrolysis, these features disappeared, and a new peak corresponding to the —NH— group of H_2Pc emerged at a binding energy of 399.8 eV [49]. These findings indicate that CuPc decomposed during the electrolysis to form H_2Pc, which is also inactive towards *e*-CO_2RR, as evidenced by no detectable CO generation in Figure S6. Note that the redeposition of Cu species onto the electrode was not observed in this study, likely due to the significantly lower Cu content (0.0046 μmol cm^{-2}) in the as-prepared MWCNT|CuPc-modified GDE compared to those (≥0.1 μmol cm^{-2}) reported previously [49, 51, 52]. However, incorporating a small amount of CuPc significantly enhanced *e*-CO_2RR activity. Specifically, the overpotential (η) required for the MWCNT|CuPc-CoPc (r = 0.5)-modified GDE required to sustain the applied current density of −100 mA cm^{-2} was about −0.77 V, which is about 70 mV less than that for the MWCNT|CoPc-modified GDE. The XPS analyses, shown in Figure 6 and Figure S9, reveal a decrease in the Co(II) and —C═N—Co peak intensities for the MWCNT|CoPc-modified GDE decreased after 2-h electrolysis, indicating the loss of Co(II) species or demetallization [53]. On the other hand, the Cu(II) $2p_{3/2}$ and Cu(II) $2p_{1/2}$ peaks at binding energies of 935.2 and 954.9 eV of the MWCNT|CuPc-CoPc (r = 0.5)-modified GDE disappeared after 2-h electrolysis, consistent with the decomposition of CuPc into H_2Pc as observed in Figure S8. However, the intensity of the Co(II) peak of the MWCNT|CuPc-CoPc (r = 0.5)-modified GDE after 2-h electrolysis remained unchanged after electrolysis, suggesting that the reduction in overpotential by incorporating a small amount of CuPc is beneficial to mitigate CoPc deactivation caused by the undesirable reduction of the Pc ligands at highly cathodic potential [27]. Notably, the MWCNT|CuPc-CoPc (r = 0.5)-modified GDE exhibited significantly improved FE_{CO} (71.0 ± 9.1% vs. 47.2 ± 1.9%) and TOF_{CO} (26.66 ± 3.41 s^{-1} vs. 16.02 ± 0.65 s^{-1}) compared to the MWCNT|CoPc-modified GDE (Figure 5). Note that, as CuPc itself is inactive towards *e*-CO_2RR, the TOF_{CO} values were calculated based solely on the ICP-OES-determined CoPc content. In contrast, the MWCNT|CuPc-CoPc (r)-modified GDE with r value ≥1 required significantly high overpotential (η >0.84 V) to sustain the applied current density of −100 mA cm^{-2}, presumably due to a lower amount of active CoPc, leading to pronounced deactivation (Figure S7). Moreover, as revealed in Figure 6, the Co $2p_{1/2}$ and Co $2p_{3/2}$ peaks of the MWCNT|CuPc-CoPc (r = 0.5)- and MWCNT|H_2Pc-CoPc (r = 0.5)-modified GDEs shifted to a higher binding energy compared to the MWCNT|CoPc-modified GDE, indicating a lower oxidation state of Co sites in the MWCNT|CuPc-CoPc (r = 0.5)- and MWCNT|H_2Pc-CoPc (r = 0.5)-modified GDEs. This shift suggests the presence of electronic interactions between CoPc and either CuPc or H_2Pc, which enrich the electron density of the Co active site and thereby facilitate CO_2 adsorption and activation [34, 46, 48, 54].

The electrochemically available CoPc (τ_{CoPc}) and θ on the prepared electrodes were quantified using cyclic voltammetry (CV) and ICP-OES (see Experimental Section for the details), and

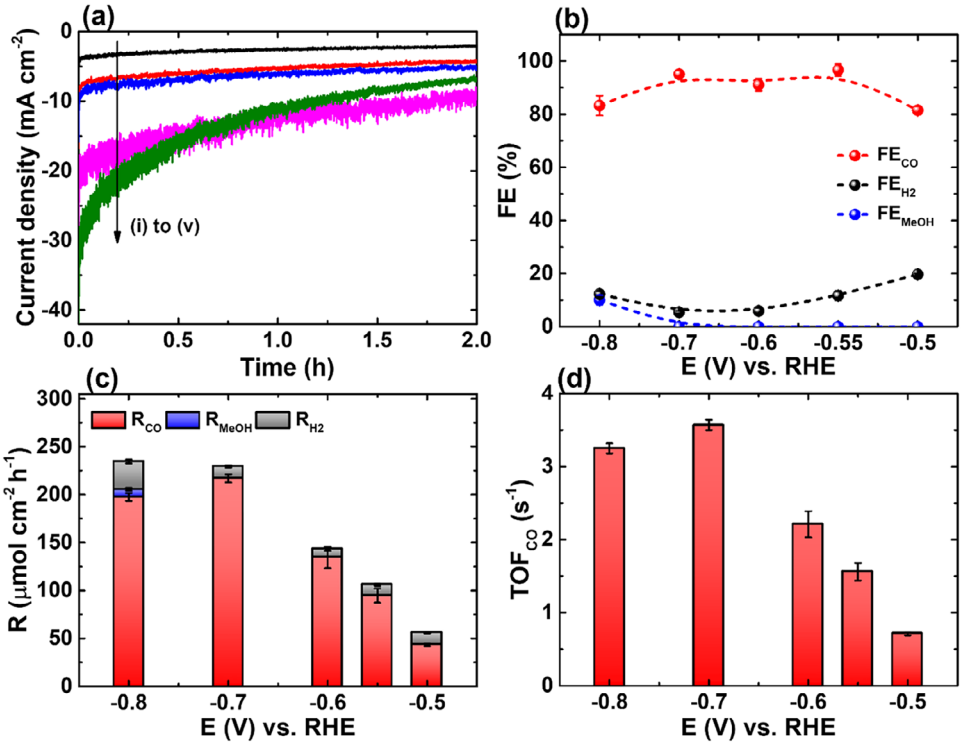

FIGURE 4 | The *e*-CO_2RR performance of the MWCNT|CoPc electrode (catalyst loading was 0.1 mg cm^{-2}) obtained from 2-h electrolysis experiments at various applied potentials (i: −0.5 V; ii: −0.55 V; iii: −0.6 V; iv: −0.7 V; v: −0.8 V vs. RHE) in $NaHCO_3$ (0.5 M) solution under 98% CO_2 atmosphere: (a) Current transients, (b) FE of products, (c) generation rate (R) of products, and (d) TOF_{CO}. The reported standard deviation was calculated from a minimum of three repeated experiments.

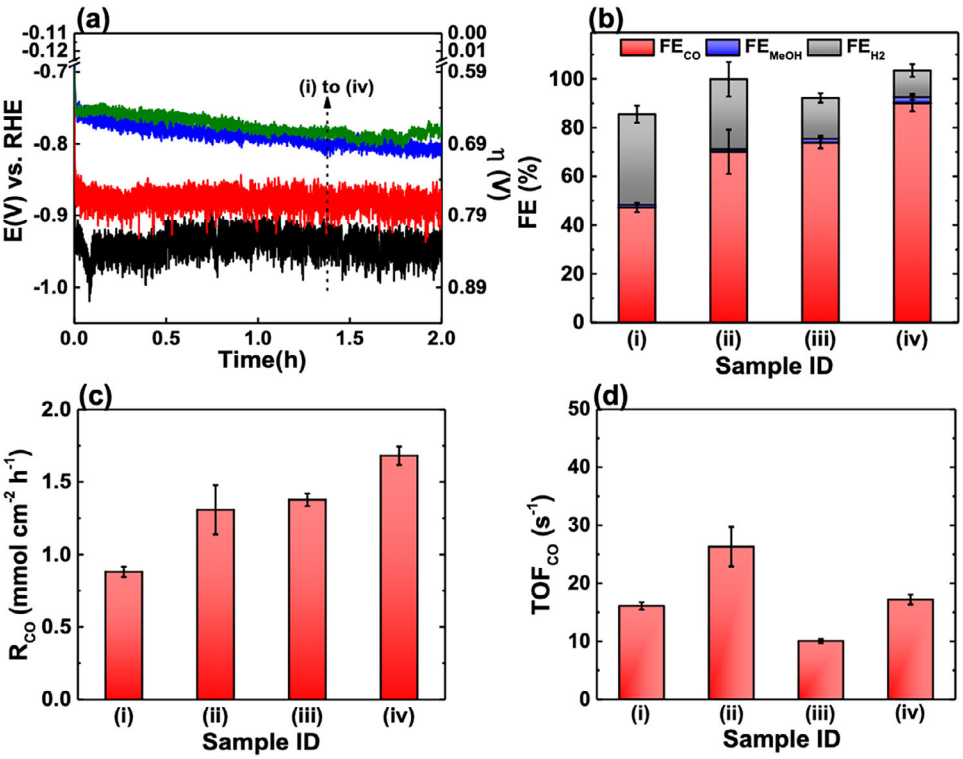

FIGURE 5 | The *e*-CO_2RR performance of the MWCNT|CoPc-modified GDE (i and iii) and MWCNT|CuPc-CoPc (r = 0.5)-modified GDE (ii and iv) obtained from 2-h electrolysis experiments at −100 mA cm^{-2} in $KHCO_3$ (1.0 M) solution under 98% CO_2 atmosphere: (a) Potential transients, (b) FE of products, (c) R_{CO}, and (d) TOF_{CO}. Catalyst loadings were 0.1 mg cm^{-2} for samples (i) and (ii), and 0.2 mg cm^{-2} for samples (iii) and (iv). The reported standard deviation was calculated from a minimum of three repeated experiments.

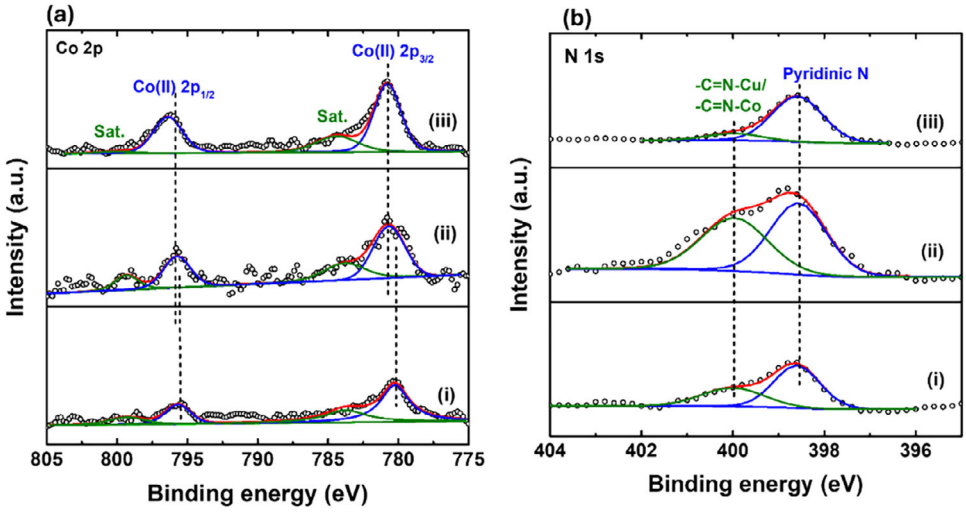

FIGURE 6 | (a) Cu 2p and (b) N 1s XPS spectra of (i) the as-prepared MWCNT|CoPc-modified GDE, (ii) the as-prepared MWCNT|H_2Pc-CoPc (r = 0.5)-modified GDE, and (iii) the as-prepared MWCNT|CuPc-CoPc (r = 0.5)-modified GDE.

the results are shown in Figures S10 and S11 and Table S1. As revealed, incorporating either CuPc or H_2Pc significantly influenced τ_{CoPc}. Particularly, the MWCNT|CuPc-CoPc (r = 0.5)-modified GDE and MWCNT|H_2Pc-CoPc (r = 0.5)-modified GDE exhibited τ_{CoPc} values of 3.0 and 2.8 nmol cm^{-2}, respectively, both exceeding that obtained for the MWCNT|CoPc-modified GDE (1.9 nmol cm^{-2}). Similarly, the incorporation of CuPc or H_2Pc was significantly enhanced θ, with the MWCNT|CuPc-CoPc (r = 0.5)- and MWCNT|H_2Pc-CoPc (r = 0.5)-modified GDEs reaching values of 0.22 and 0.21, respectively, both exceeding that (0.12) observed for the MWCNT|CoPc control. These findings suggest that incorporating a small amount of CuPc or H_2Pc effectively mitigated CoPc aggregation, thereby increasing the accessibility of the active CoPc sites for *e*-CO_2RR. This molecular-level dispersion of CoPc is achieved by mitigating CoPc aggregation through both steric hindrance and electronic modulation, arising from delocalized π coordination [34, 54–57] induced by the incorporation of CuPc or H_2Pc molecules. The presence of steric hindrance prevents aggregation among CoPc, while the electron transfer between the central metal Co in CoPc and the central metal Cu in CuPc disrupts the π–π stacking interactions among the CoPc molecules. The underlying mechanism is schematically illustrated in Scheme 1. The uniform distribution of the isolated CoPc (atomic radius: 0.19 nm) and CuPc (atomic radius: 0.14 nm) on the as-prepared MWCNT|CuPc-CoPc (r = 0.5)-modified GDE was further confirmed by the HAADF-STEM and STEM-EDS analyses (Figure 7a–c). Furthermore, CO_2-TPD analysis (Figure 7d) reveals that MWCNT|CuPc-CoPc(r = 0.5) exhibited desorption peaks of CO_2 at 115°C, 204°C, and 260°C, having a higher total CO_2 adsorption capacity (91.5 vs. 73 μmol CO_2 g^{-1}) compared to MWCNT|CoPc control. The enhancement corroborates that the incorporation of CuPc effectively increased the accessibility of the active CoPc site, thereby facilitating superior CO_2 adsorption.

It is interesting to note that θ of the MWCNT|CuPc-CoPc (r = 0.5)-modified GDE increased from 0.22 to 0.32 after potential cycling between 0.66 and −0.84 V vs. RHE for 10 cycles in $KHCO_3$ solution (1.0 M) (Figure S12). XPS analysis (Figure S8) revealed CuPc decomposed to form H_2Pc at potentials ≥−0.84 V, suggesting such decomposition would facilitate the exposure of previously buried CoPc active sites during electrolysis. To elucidate the underlying mechanism, density functional theory (DFT) calculations were performed using coaxially stacked bilayer models, as shown in the inset in Figure 8a. These models consist of two CoPc units (CoPc-CoPc) or a CoPc unit paired with a CuPc unit (CoPc-CuPc) or H_2Pc unit (CoPc-H_2Pc). The d-band center (ε_d), a key descriptor for the binding strength between intermediate species and the active sites, was calculated from the partial density of state (pDOS), as shown in Figure 8a. As revealed, the pristine CoPc exhibited a ε_d of −1.08 eV, which downshifted significantly upon incorporation of CuPc (−1.61 eV) or H_2Pc (−1.67 eV). According to the Sabatier principle, catalytic efficiency is maximized at an optimal adsorption strength; adsorption that is either too strong or too weak hinders reaction kinetics [58, 59]. These results indicate that CoPc binds intermediates too strongly, whereas the addition of CuPc or H_2Pc moderates this interaction to a more favorable level. The CuPc-CoPc catalyst, with its optimized d-band position, achieves the ideal balance, leading to the superior FE_{CO} observed experimentally. Furthermore, the calculated adsorption energy of CO_2 ($E_{ads,CO2}$) for CoPc-CuPc (−0.19 eV) and CoPc-H_2Pc (−0.20 eV) was less negative than that for CoPc-CoPc (−0.24 eV) (Figure 8b), indicating a weakening of CO_2 binding after the incorporation of CuPc or H_2Pc. This theoretical finding perfectly corroborates our TPD analyses (Figure 3 and 7d), where the CO_2 desorption peak maximum for MWCNT|CuPc-CoPc (r = 0.5) appeared at a lower temperature relative to the MWCNT|CoPc control (204°C vs. 224°C). Interestingly, while MWCNT|CuPc-CoPc (r = 0.5) exhibited lower CO_2 binding strength compared to the MWCNT|CoPc control, it possessed a higher total CO_2 adsorption capacity (91.5 vs. 73 μmol CO_2 g^{-1}) than the MWCNT|CoPc control. This enhancement is attributed to the increased accessibility of the active CoPc sites, as the incorporation of CuPc helps mitigate CoPc aggregation, thereby exposing more active surface area. Taken together, the enhanced *e*-CO_2RR performance of the MWCNT|CuPc-CoPc (r = 0.5)-modified GDE can be attributed to favourable electronic interactions between CoPc and CuPc and/or H_2Pc formed via CuPc decomposition, as well as the improved accessibility of CoPc active sites. Notably, the molecular-level dispersion enabled a

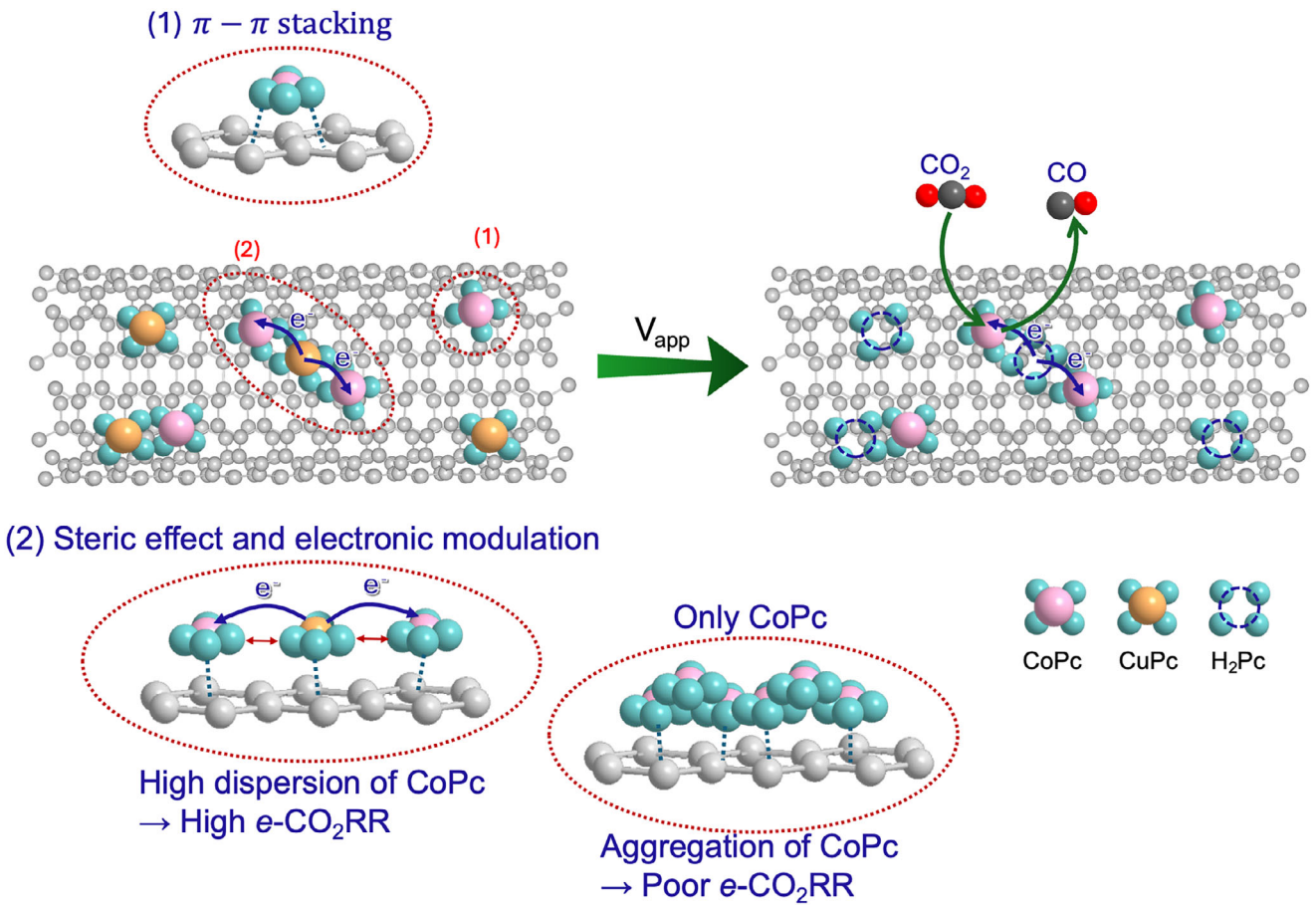

SCHEME 1 | The proposed mechanism of the enhanced e-CO_2RR performance of the MWCNT|CuPc-CoPc (r = 0.5). The dashed line indicates the π–π stacking. The blue and red arrows indicate the electron transfer and the steric effect, respectively.

high intrinsic e-CO_2RR activity with a τ_{CoPc}-based e-TOF_{CO} of 121.18 ± 15.50 s^{-1}.

To mitigate deactivation associated with the high overpotential required to maintain the applied current density of −100 mA cm^{-2}, additional MWCNT|CoPc-, MWCNT|CuPc-CoPc (r = 0.5)-, and MWCNT|H_2Pc-CoPc (r = 0.5)-modified GDEs were prepared with an increased catalyst loading (0.2 mg cm^{-2}) and subjected to the 2-h electrolysis. The results, shown in Figure 5, indicate that increasing the catalyst loading effectively reduced the overpotential, presumably by increasing the number of active sites, and thus enhanced FE_{CO} of both MWCNT|CoPc- and MWCNT|CuPc-CoPc (r = 0.5)-modified GDEs. Specifically, FE_{CO} improved from 47.2 ± 1.9% to 73.8 ± 2.3% for the MWCNT|CoPc-modified GDE, and from 71.0 ± 9.1% to 90.1 ± 3.4% for the MWCNT|CuPc-CoPc (r = 0.5)-modified GDE. Furthermore, as revealed in Figure S13, the MWCNT|CuPc-CoPc (r = 0.5)-modified GDE exhibited excellent stability during prolonged electrolysis at −100 mA cm^{-2}, maintaining a high FE_{CO} (~91.2%), a TOF_{CO} (15.74 s^{-1}), and cathodic energy efficiency for CO production (EE_{CO}: 68.9%), defined as the ratio of chemical energy stored in CO to applied electrical energy (see Experimental Section for the details), over 12 h electrolysis. Moreover, as revealed in Figure 5 and Figure S14, the MWCNT|H_2Pc-CoPc (r = 0.5)-modified GDE exhibited better e-CO_2RR performance, in terms of FE_{CO} (77.7 ± 4.9% vs. 73.8 ± 2.3%) and TOF_{CO} (14.91 ± 0.64 s^{-1} vs. 10.05 ± 0.32 s^{-1}), than the MWCNT|CoPc-modified GDE. This finding is in agreement with the previous discussion that the enhanced e-CO_2RR performance of the MWCNT|CuPc-CoPc (r = 0.5)-modified GDE can be attributed to favourable electronic interactions between CoPc and CuPc and/or H_2Pc formed via CuPc decomposition during electrolysis, as well as the improved accessibility of CoPc active sites. The enhanced τ_{CoPc} and θ also promoted further reduction of CO into methanol, presumably by providing a high local CO concentration that facilitates subsequent CO reduction through a domino pathway [27]. Specifically, the MWCNT|CuPc-CoPc (r = 0.5)- and MWCNT|H_2Pc-CoPc (r = 0.5)-modified GDEs exhibited FE_{MeOH} of 2.5 ± 1.2%, and 4.2 ± 1.7%, respectively, both outperforming the MWCNT|CoPc control. We also prepared the MWCNT|NiPc-CoPc (r = 0.5)-modified GDE for performance comparison. As revealed in Figure S15 and Figure 5, the MWCNT|NiPc-CoPc (r = 0.5)-modified GDE exhibited inferior performance than the MWCNT|CoPc-modified GDE, requiring a significantly higher overpotential (~−0.80 vs. −0.70 V) to sustain the applied current density and yielding a lower FE_{CO} (71.8 ± 8.4% vs. 73.8 ± 2.3%). This finding stands in sharp contrast to the MWCNT|CuPc-CoPc (r = 0.5)-modified GDE and can be attributed to the lower e-CO_2RR activity of NiPc than CoPc and its inability to decompose into H_2Pc during e-CO_2RR [60], thereby lacking the synergistic electronic interactions required for performance enhancement. Note that further increase in catalyst loading for the electrode preparation was not attempted as the marginal gains in FE_{CO} were offset by a substantial decline in TOF_{CO}.

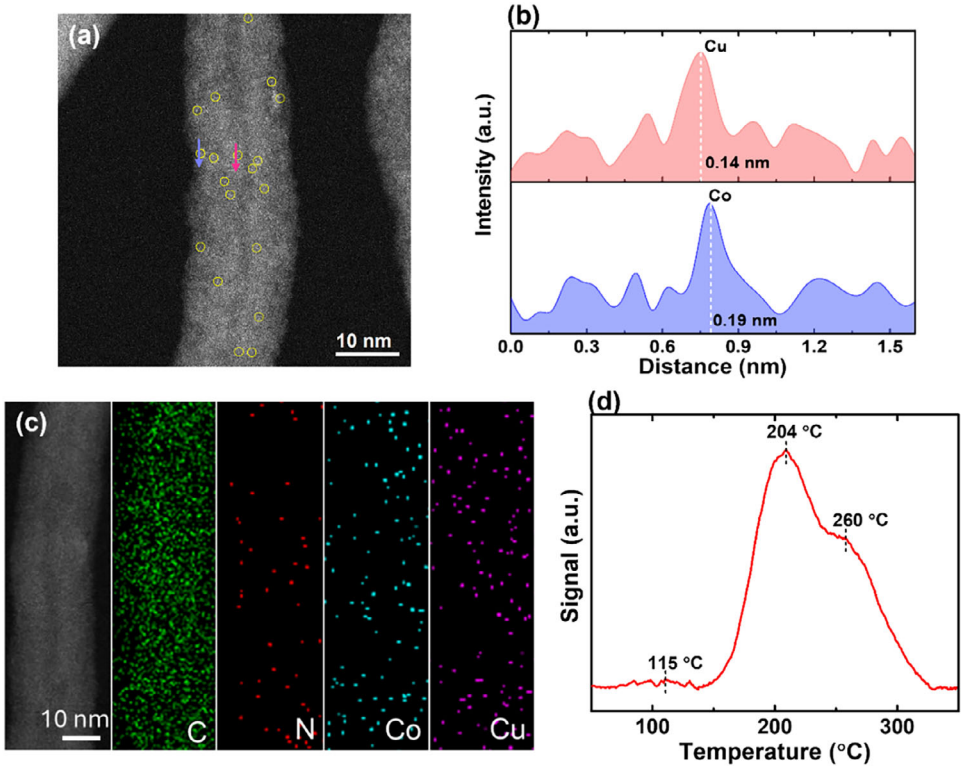

FIGURE 7 | (a) HAADF-STEM image, (b) line profiles along the blue and red arrows in (a), and (c) STEM-EDS elemental mapping of the MWCNT|CuPc-CoPc (r = 0.5)-modified GDE. (d) CO_2-TPD profiles of MWCNT|CuPc-CoPc (r = 0.5).

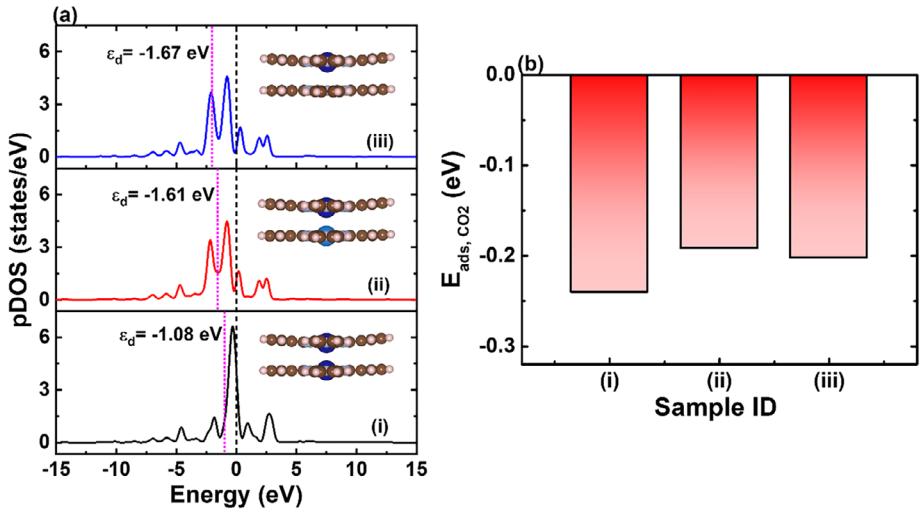

FIGURE 8 | (a) pDOS of Co 3d orbital of (i) CoPc-CoPc, (ii) CuPc-CoPc, and (iii) H_2Pc-CoPc. The Fermi level is set to zero, indicated by a black dashed vertical line. The pink dashed vertical lines represent the ε_d energy level. (b) $E_{ads,\ CO2}$ for (i) CoPc-CoPc, (ii) CuPc-CoPc, and (iii) H_2Pc-CoPc.

Figure 9 and Figure S16 show the *e*-CO_2RR performance of the MWCNT|CuPc-CoPc (r = 0.5)-modified GDE at an applied current of 6.25 A (or −100 mA cm^{-2}) under CO_2 atmospheres of various CO_2 concentrations (10%~98%). As revealed, the FE_{CO} and cathodic energy efficiency (EE_{CO}) for CO generation of the MWCNT|CuPc-CoPc (r = 0.5)-modified GDE remained above 80% and 50%, respectively, even when the CO_2 concentration was reduced to 20%. Specifically, the MWCNT|CuPc-CoPc (r = 0.5)-modified GDE exhibited a FE_{CO} of 92.6 ± 1.3% and an EE_{CO} of 62.2 ± 0.8% under 40% CO_2 atmosphere at −0.76 V vs. RHE, and a FE_{CO} of 80.4 ± 2.8% and an EE_{CO} of 54.8 ± 1.9% under 20% CO_2 atmosphere at −0.82 V vs. RHE. This high CO selectivity of the MWCNT|CuPc-CoPc (r = 0.5)-modified GDE from the conversion of low-concentration CO_2 is likely attributed to the enhanced CO_2 adsorption capability (e.g., Figure 7d) and moderate binding strength of CO_2 resulting from favourable electronic interactions among MWCNT, CoPc, CuPc, and H_2Pc formed in situ via CuPc decomposition during electrolysis, along with the improved accessibility of CoPc active sites. Additionally, the high FE_{CO} at low CO_2 concentrations enabled efficient

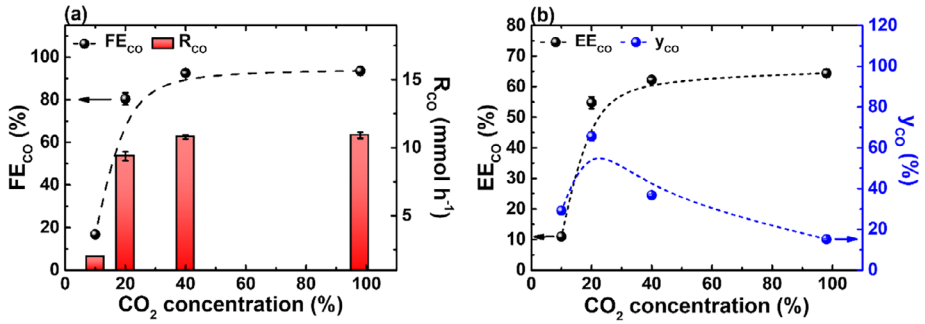

FIGURE 9 | The *e*-CO_2RR performance of the MWCNT|CuPc-CoPc (r = 0.5)-modified GDE at −100 mA cm^{-2} in $KHCO_3$ (1.0 M) solution under CO_2 atmospheres of various concentrations: (a) FE of products and R_{CO}, and (b) EE_{CO} and y_{CO}. Catalyst loading was 0.2 mg cm^{-2}. The reported standard deviation was calculated from a minimum of three repeated experiments.

single-pass CO_2 conversion and high CO yield. Notably, it is the first time that a high CO yield of 65.7 ± 2.3% from the conversion of low-concentration CO_2 has been realized using a molecular catalyst-based modified electrode. Furthermore, as revealed from Figure S17, the MWCNT|CuPc-CoPc (r = 0.5)-modified electrode remains its high e-CO_2RR performance in the presence of H_2S. Specifically, the MWCNT|CuPc-CoPc (r = 0.5)-modified electrode maintained a FE_{CO} >93.5% throughout the electrolysis with the gas feed containing 98% CO_2 and 2% H_2S, outperforming the MWCNT|CoPc control (FE_{CO} <86%). The enhanced FE_{CO} is corroborated by the increased CO_2 adsorption capacity (91.5 vs. 73 μmol CO_2 g^{-1}) of the MWCNT|CuPc-CoPc (r = 0.5)-modified electrode compared to the MWCNT|CoPc control. Moreover, the MWCNT|CuPc-CoPc (r = 0.5)-modified GDE also exhibited high stability under simulated biogas atmosphere, maintaining a FE_{CO} > 80% over 72-h electrolysis (Figure S18). The excellent *e*-CO_2RR performance MWCNT|CuPc-CoPc (r = 0.5)-modified GDE was attributed to its sustaining molecular-dispersion of the active CoPc molecules on MWCNT, as evidenced by HAADF-STEM and STEM-EDS analyses shown in Figure S19. Furthermore, the FE_{CO} of MWCNT|CuPc-CoPc (r = 0.5)-modified GDE remained above 80% and an EE_{CO} of 53.4 ± 1.4% under 40% CO_2 atmosphere at a higher applied current density of −200 mA cm^{-2} at the expense of applied potential of −0.81 V vs. RHE (Figure S20). The excellent *e*-CO_2RR performance of the developed MWCNT|CuPc-CoPc (r = 0.5)-modified GDE under a broad range of CO_2 concentrations and high current density places itself among the most active CoPc- and cobalt-porphyrin-based systems reported to date (Table S2). This finding highlights the effectiveness of CuPc incorporation in enhancing CO_2 affinity and electrochemically available CoPc active sites, thereby boosting the e-CO_2RR performance of the MWCNT|CuPc-CoPc (r = 0.5)-modified GDE, particularly for the conversion of low-concentration CO_2. Collectively, these findings highlight the promise of this molecularly engineered system for future industrial deployment, particularly in scalable CO_2 electroreduction platforms targeting efficient and selective CO production to support carbon mitigation and the circular economy initiatives.

3 | Conclusion

The MWCNT|CuPc-CoPc (r)-modified GDEs, featuring the molecular-level dispersion of CoPc and CuPc on the MWCNT support, were successfully prepared using a simple H_2SO_4-assisted impregnation method. The incorporation of CuPc or H_2Pc effectively suppressed CoPc aggregation, enabling tunable loading and fractional accessibility of electrochemically active CoPc sites. In particular, the MWCNT|CuPc-CoPc (r = 0.5)-modified GDE exhibited significantly-enhanced θ of 0.32, attributed to the in situ decomposition of CuPc during electrolysis, which facilitated the exposure of previously buried CoPc active sites. The enhanced accessibility of CoPc active sites, along with the optimized binding strength, attributed to the favourable electronic interactions among CoPc, MWCNT, CuPc, and H_2Pc formed in situ via CuPc decomposition during electrolysis, remarkably boosted the e-CO_2RR performance of the MWCNT|CuPc-CoPc (r = 0.5)-modified GDE, especially for the conversion of low-concentration CO_2. Notably, it is the first time that a high y_{CO} of 65.7 ± 2.3% from single-pass conversion of 20% CO_2 at Ampere-level current has been realized using a molecular catalyst-based modified electrode. Furthermore, the high stability of the MWCNT|CuPc-CoPc (r = 0.5)-modified GDE, maintaining a FE_{CO}>80.4% over 72-h electrolysis under simulated biogas atmosphere, was also demonstrated. The DFT calculation revealed that CuP modulates ε_d position of the catalyst, resulting in optimal binding energy for reaction intermediates. This electronic tuning facilitates the interaction with the Co active sites, thereby promoting CO_2 conversion to CO. These findings demonstrate the strong promise of the developed molecularly engineered catalyst system in promoting carbon neutrality through efficient and selective CO production from low-concentration CO_2 emission sources.

4 | Experimental Section/Methods

4.1 | Chemical and Materials

All the chemicals used for the preparation of catalytic materials, modified electrodes, and electrolyte solutions, including cobalt (II) phthalocyanine (CoPc; 97%, Sigma–Aldrich), copper (II) phthalocyanine (CuPc; Cu content >80%, Honeywell Fluka), 29H, 31H-phthalocyanine (H_2Pc; 98%, Sigma–Aldrich), nickel (II) phthalocyanine (NiPc; 95%, Acros Organic), sodium sulfide hydrate (60%–64%, extra pure flakes, Thermo Scientific), dimethylformamide (DMF; 99.8%, TEDIA), multi-walled carbon nanotubes (MWCNT; >95% carbon, Sigma–Aldrich), sulfuric acid (≥97%, Honeywell Fluka), potassium hydroxide (≥85%,

Honeywell Fluka), hydrogen chloride (≥37%, Honeywell Fluka), $NaHCO_3$ (≥98%, Sigma–Aldrich), $KHCO_3$ (99%, Alfa Aesar), $CsHCO_3$ (99.99%, Macklin), Nafion 117 solution (5wt.%, Sigma–Aldrich), and ethanol (≥99.5%, Echo Chemical) were purchased from commercial suppliers and used without additional purification. Deionized water (DIW; 18.2 MΩ•cm) was used for the electrode rinsing and electrolyte preparation throughout the work. Nickel foam (>99%, thickness: 1 mm) was obtained from Central Research Company, Taiwan. Before use, Ni foam was cleaned by immersion in HCl (1 M) for 5 min, followed by thorough rinsing with DIW. GDL-340 carbon paper (thickness of 340 μm) with a microporous layer, used as the gas diffusion electrode (GDE) substrate, was purchased from CeTech Co., Ltd., Taiwan. The GDE substrate was cleaned by immersion in HCl (~10 M) for 5 min, followed by thorough rinsing with DIW.

4.2 | Synthesis of MWCNT-Supported Metal Phthalocyanines

MWCNT-supported CoPc and CuPc with various nominal CuPc/CoPc weight ratios (r), designated as MWCNT|CuPc-CoPc (r) for simplicity, were synthesized by firstly preparing a dispersion solution containing CoPc, CuPc, and MWCNTs by dispersing 9/(1+r) mg CoPc, 9r/(1+r) CuPc, and 45 mg MWCNT in 45 mL H_2SO_4 under ultrasonication for 1 h and subsequent continuous stirring for an additional 2 h. The resulting dispersion solution was then slowly poured into ice-cooled DIW and subjected to repeated centrifugations and washing with deionized water and ethanol until the pH of the supernatant reached 7. Finally, the precipitate was then dried in an oven at 60°C overnight. MWCNT|H_2Pc-CoPc (r = 0.5) and MWCNT|NiPc-CoPc (r = 0.5) were also prepared with the same procedure described above by replacing CuPc with H_2Pc or NiPc.

MWCNT-supported CoPc (i.e., MWCNT|CoPc), MWCNT-supported CuPc (i.e., MWCNT|CuPc), and MWCNT-supported phthalocyanine (i.e., MWCNT|H_2Pc), were prepared with the same procedure described above. Nevertheless, the dispersion solutions for the preparation of MWCNT|CoPc, MWCNT|CuPc, and MWCNT|H_2Pc were prepared by dispersing 9 mg CoPc, 9 mg CuPc, and 9 mg H_2Pc, in 45 mL H_2SO_4 containing 45 mg MWCNT, respectively.

4.3 | Electrode Preparation

To prepare *MWCNT-supported metal phthalocyanine*-modified electrodes, catalyst inks were first prepared by dispersing 10 mg *MWCNT-supported metal phthalocyanine* (i.e., MWCNT|CuPc-CoPc (r), MWCNT|CoPc, MWCNT|CuPc, and MWCNT|H_2Pc) in 10 mL ethanol under ultrasonication for 2 h. Unless otherwise noted, an aliquot of 100 μL cm^{-2} of the catalyst ink and 1 μL cm^{-2} of Nafion 117 solution were subsequently drop-casted onto the GDE substrate (working area: 2.0 cm × 2.0 cm or 2.5 cm × 2.5 cm).

4.4 | Physical Characterization

The loading amounts of CoPc and CuPc in the prepared electrodes were quantified by inductively-coupled plasma optical emission spectrometry (ICP-OES; Horiba Jobin Yvon JY2000-2). The chemical composition of the prepared electrodes was characterized by X-ray photoelectron spectroscopy (XPS) using a PHI 5000 VersaProbe system (ULVAC-PHI, Chigasaki, Japan). The binding energy (BE) scale of the acquired XPS spectra was calibrated against the Au^0 $4f_{7/2}$ peak of the deposited gold nanoparticles at 84.0 eV. The particle size of the dispersed CoPc was determined by dynamic light scattering (DLS) using a Malvern Zetasizer Nano ZS particle size analyser (Malvern Instruments Ltd., Worcestershire, UK). The CO_2-TPD measurement was carried out using AutoChem II (Micromeritics), equipped with a thermal conductivity detector. Following CO_2 purging, the TPD profile was recorded with a He stream (25 mL min^{-1}) as the sweeping gas at a heating rate of 10°C min^{-1}. Detailed structural and elemental analyses of MWCNT|CuPc-CoPc (r = 0.5) and MWCNT|CoPc were performed by transmission electron microscopy and HAADF-STEM using a JEM-2100F microscope (JEOL Ltd., Japan). SEM images were obtained using Hitachi SU-8010. Raman analyses were performed using a DXR Raman spectrometer (Thermo Fisher Scientific, USA) equipped with a 532 nm laser.

4.5 | Electrochemical Characterization

The electrochemical characterizations on the *e*-CO_2RR performance of the MWCNT-supported metal phthalocyanine-modified electrodes were performed in the homemade two-compartment H-cell or flow-type electrolyzer (Scheme S1) connecting to an Ivium-n-Stat multichannel potentiostat (Ivium Technologies B.V., Netherlands) under a gas atmosphere containing CO_2 of various concentrations (10%–98%). The anodic and cathodic compartments of the H-cell and flow-type electrolyzer were separated with a Neosepta ASE anion exchange membrane (ASTOM Corporation, Tokyo, Japan). In the case of the electrochemical characterization with the two-compartment H-cell, the MWCNT-supported metal phthalocyanine-modified electrodes (geometry area of 0.5 cm^2) were used as the working electrode and placed with an Ag/AgCl (sat'd KCl) reference electrode in the cathodic compartment, whereas a Pt foil (2 cm × 1 cm) counter electrode was placed in the anodic compartment. In the case of the electrochemical characterization with the flow-type electrolyzer, the MWCNT-supported metal phthalocyanine-modified electrodes (geometry area of 4.0~6.25 cm^2) were used as the working electrode and placed with Ag/AgCl (sat'd KCl) reference electrode in the cathodic compartment, whereas a nickel foam (3.5 cm × 3.5 cm) counter electrode was placed in the anodic compartment. The catalyst loading was 0.1~0.2 mg cm^{-2} for both the H-cell and the flow-type electrolyzer, unless otherwise stated. CO_2 concentration (C_{CO2}) was regulated by adjusting the relative flow rates of the CO_2/Ar gas stream (98% CO_2 and 2% Ar; Yun Shan Gas Co., Taiwan) and high-purity Ar gas stream (99.995%; Yun Shan Gas Co., Taiwan) using a mass flow controller. The simulated biogas environment was created by purging the cathodic compartment with the CO_2/CH_4 gas mixture (40% CO_2 and 60% CH_4; Yun Shan Gas Co., Taiwan). To investigate the effects of H_2S, the electrolysis experiments were performed with the feed of 98% CO_2 and 2% H_2S. In this setup, H_2S gas was generated in situ by the acidification of a sodium sulfide solution (~10 wt.%) with a HCl solution (1.67 M). Unless otherwise noted, the total flow rate (ϕ) was maintained at 35 mL min^{-1}. The

$KHCO_3$ solution (1.0 M) was used as the catholyte, whereas KOH (1 M) solution was used as the anolyte. Both the catholyte and anolyte were circulated respectively to the cathodic and anodic compartments of the flow-type electrolyzer at a flow rate of 35 mL min^{-1} using peristaltic pumps. 95% IR compensation was used for all electrochemical measurements. Unless otherwise noted, the potentials reported in this work are referenced to the reversible hydrogen electrode (RHE) according to Equation 1:

$$E\ (V\ vs.\ RHE) = E\ (V\ vs.\ Ag/AgCl) + 0.197 + 0.059 \times pH \quad (1)$$

The overpotential (η) for the generation of CO from *e*-CO_2RR was defined as the difference between the applied potential and the equilibrium potential for CO_2 reduction to CO (i.e., −0.11 V vs. RHE). The electrochemically accessible amount of CoPc (τ_{CoPc}) in the prepared electrodes was quantified using cyclic voltammetry (CV) in $NaHCO_3$ solution (1 M). Briefly, the values of peak current density (I_p) responsible for the redox reaction of Co^{2+}/Co^{+} (*i.e.*, O_1/R_1 redox peaks in Figures S10a–e) in CoPc at various scan rates (v) were first determined. Thereafter, τ was deduced from the slope of the I_p vs. v plot using Equation 2:

$$I_p = \frac{n^2F^2\tau_{CoPc}}{4RT}v \quad (2)$$

where n is the number of electron transfer number for the redox reaction of Co^{2+}/Co^{+}, F is the Faraday constant (96485 C mol^{-1}), R is the ideal gas constant (8.314 J K^{-1} mol^{-1}), and T is the operating temperature (300 K). The ratio of the electrochemically accessible amount of CoPc to the loading amount of CoPc (N_{CoPc}), quantified by ICP-OES, was used to evaluate the fraction of electrochemically available CoPc on the prepared electrodes (θ) using Equation 3:

$$\theta = \tau_{CoPc}/N_{CoPc} \quad (3)$$

4.6 | Product Analysis and Quantification

The main liquid products (*i.e.*, methanol) produced from the electrolysis experiments were analyzed and quantified using a Shimadzu GC-2010 Plus gas chromatography system (GC) equipped with a Rtx-Volatiles column and a flame ionization detector (FID). The GC oven temperature was initially held at 40°C for 1 min, then ramped at 40°C min^{-1} to 80°C and maintained at 80°C for 6 min, and finally ramped at 20°C min^{-1} to 250°C and held for an additional 8.5 min. Gaseous products generated from the electrolysis experiments, on the other hand, were analyzed and quantified using an Agilent 7890B Series gas chromatography system. CO was detected using a Carboxen-1006 PLOT column with helium as the carrier gas at a flow rate of ∼5 mL min^{-1}, coupled to a thermal conductivity detector (TCD) and a flame ionization detector (FID) connected in series. Hydrogen gas was analyzed using an HP-PLOT Molesieve 19095P-MS6 column with nitrogen as the carrier gas at a flow rate of ∼4 mL min^{-1}, coupled to a TCD detector. The GC oven temperature for both the Carboxen-1006 PLOT and HP-PLOT Molesieve columns was initially maintained at 40°C for 8 min, ramped at 40°C min^{-1} to 200°C, and then held at 200°C for an additional 8 min. The concentrations of obtained products ($C_{product}$) were determined by converting the measured TCD and FID signals with routinely updated calibration curves. For the quantification of CO generated from e-CO_2RR under a feed of 98% CO_2 and 2% H_2S, the cathodic headspace was monitored using a portable MET-GD4AP gas detector (S.E.A.T. Industry Technology Co., Ltd) to the headspace of the cathodic compartment with a sampling pump. The Faradaic efficiency of product ($FE_{product}$) obtained from the electrolysis experiments using the two-compartment H-cell and the flow-type electrolyzer was determined by Equations 4 and 5, respectively.

$$FE_{product} = \frac{C_{product} \times V \times n_{product} \times F}{Q_{total}} \times 100\% \quad (4)$$

$$FE_{product} = \frac{R_{product} \times n_{product} \times F}{J} = \frac{\phi \times C_{product} \times \frac{P}{RT} \times n_{product} \times F}{J} \times 100\% \quad (5)$$

where V is volume of headspace (for gaseous product) or volume of catholyte (for liquid product), $n_{product}$ is the number of electrons transferred for the formation of the specific product, Q_{total} is the total charge passed in the electrolysis, $R_{product}$ is the generation rate of specific product, P is the ambient pressure, R is the ideal gas constant (8.314 J K^{-1} mol^{-1}), T is the operating temperature (300 K), F is the Faradaic constant (96 485 C mol^{-1}), and J is the applied current density.

The CO yield (y_{CO}) at specific CO_2 feeding rate (F_{CO2}) was calculated using Equation 6:

$$y_{CO} = \frac{R_{CO}}{F_{CO_2}} = \frac{j \times C_{CO} \times \frac{P}{RT}}{j \times C_{CO_2} \times \frac{P}{RT}} = \frac{C_{CO}}{C_{CO_2}} \quad (6)$$

The EE_{CO}, defined as the ratio of chemical energy stored in CO to applied electrical energy, was determined using Equation 7: [61]

$$EE_{CO} = \frac{\left(1.23 - E^0_{CO}\right) \times FE_{C_{CO}}}{1.23 - E_{app}} \times 100\% \quad (7)$$

where E^0_{CO} is the standard reduction potential for the generation of CO (−0.1 V vs. RHE) from *e*-CO_2RR, and E_{app} is the operation potential under a specific applied current density.

Two kinds of turnover frequencies were used to evaluate the *e*-CO_2RR activity of the prepared electrodes, including one based on N_{CoPc} (TOF_{CO}) and the other based on τ_{CoPc} (*e*-TOF_{CO}). TOF_{CO}, determined by using Equation (8), was used to evaluate the overall activity, whereas *e*-TOF_{CO}, determined by using Equation (9) [62], was used to assess the intrinsic activity.

$$TOF_{CO} = \frac{R_{CO}}{N_{CoPc}} \quad (8)$$

$$e - TOF_{CO} = \frac{R_{CO}}{\tau_{CoPc}} \quad (9)$$

4.7 | DFT Calculation

First-principles calculations based on Density Functional Theory (DFT) were performed using the CASTEP module [63] implemented in BIOVIA Materials Studio 2020. Spin-polarized calculations were employed, and dispersion interactions were accounted for using the Tkatchenko–Scheffler DFT-D correction [64, 65]. The exchange–correlation interactions were described within the generalized gradient approximation [66] using the Perdew–Burke–Ernzerhof functional [67]. Core–valence interactions were treated using on-the-fly generated ultrasoft pseudopotentials [68]. Geometry optimizations were carried out without symmetry constraints until the maximum force, total energy change, and atomic displacement converged below 2.0×10^{-3} Ha Å^{-1}, 1.0×10^{-5} Ha, and 5.0×10^{-3} Å, respectively. The self-consistent field (SCF) convergence criterion was set to 1.0×10^{-6} Ha. A cutoff energy of 500 eV was used for geometry optimizations. Single-point energy calculations were subsequently performed on the optimized structures using a higher cutoff energy of 550 eV with the same SCF convergence threshold. Solvent effects were considered using the Conductor-like Screening Model (COSMO) implicit solvation model with water as the solvent (dielectric constant $\varepsilon = 78.54$).

The d-band center (ε_d)was determined by Equation 10.

$$\varepsilon_d = \frac{\int_{-\infty}^{0} E\, N(E)\, dE}{\int_{-\infty}^{0} N(E)\, dE} \tag{10}$$

where E is the energy and N(E) is the projected density of states. E represents the energy relative to the Fermi level, and N(E) is the projected density of states (PDOS) for the d-orbitals of the active metal center.

The adsorption energy of CO_2 ($E_{ads,\,CO2}$) was calculated using Equation 11:

$$E_{ads,CO2} = E_{M1Pc+M2Pc+CO_2} - \left(E_{M1Pc+M2Pc} + E_{CO_2}\right) \tag{11}$$

where $E_{M1Pc+M2Pc+CO_2}$, $E_{M1Pc+M2Pc}$, and E_{CO_2} represent the total energies of MPc molecules with adsorbed CO_2, the stacked M_2Pc on M_1Pc system, and an isolated CO_2 molecule, respectively.

4.8 | Statistical Analysis

The data were reported as mean value ± standard deviation. The reported standard deviation was calculated from a minimum of three independent repeated experiments.

Acknowledgements

This research was financially supported from the National Science and Technology Council of Taiwan (114-2221-E-006-036-MY3, 114-2811-E-006-014-MY3, and 111-2221-E-006-019-MY3). This work was financially supported by the Center for Resilience and Intelligence on Sustainable Energy Research (RiSER) of National Cheng Kung University, from the framework of the Higher Education Sprout Project by the Ministry of Education (MOE) in Taiwan. The authors would also like to thank the use of ESCA003200 and EM000800, belonging to the Core Facility Center of National Cheng Kung University.

Conflicts of Interest

The authors declare no conflicts of interest.

Data Availability Statement

The data that support the findings of this study are available in the supplementary material of this article.

References

1. K. P. Kuhl, T. Hatsukade, E. R. Cave, D. N. Abram, J. Kibsgaard, and T. F. Jaramillo, "Electrocatalytic Conversion of Carbon Dioxide to Methane and Methanol on Transition Metal Surfaces," *Journal of the American Chemical Society* 136 (2014): 14107–14113, https://doi.org/10.1021/ja505791r.

2. M. He, Y. Sun, and B. Han, "Green Carbon Science: Efficient Carbon Resource Processing, Utilization, and Recycling Towards Carbon Neutrality," *Angewandte Chemie International Edition* 61 (2022): 202112835, https://doi.org/10.1002/anie.202112835.

3. Y. Xu, J. P. Edwards, J. J. Zhong, et al., "Oxygen-Tolerant Electroproduction of C_2 Products From Simulated Flue Gas," *Energy & Environmental Science* 13 (2020): 554–561, https://doi.org/10.1039/C9EE03077H.

4. S. Van Daele, L. Hintjens, J. Hoek, et al., "Influence of the Target Product on the Electrochemical Reduction of Diluted CO_2 in a Continuous Flow Cell," *Journal of CO2 Utilization* 65 (2022): 102210, https://doi.org/10.1016/j.jcou.2022.102210.

5. D. Y. C. Leung, G. Caramanna, and M. M. Maroto-Valer, "An Overview of Current Status of Carbon Dioxide Capture and Storage Technologies," *Renewable and Sustainable Energy Reviews* 39 (2014): 426–443, https://doi.org/10.1016/j.rser.2014.07.093.

6. B. U. Choi, Y. C. Tan, H. Song, K. B. Lee, and J. Oh, "System Design Considerations for Enhancing Electroproduction of Formate From Simulated Flue Gas," *ACS Sustainable Chemistry & Engineering* 9 (2021): 2348–2357, https://doi.org/10.1021/acssuschemeng.0c08632.

7. L. Y. Deng and M. B. Hagg, "Techno-Economic Evaluation of Biogas Upgrading Process Using CO_2 Facilitated Transport Membrane," *International Journal of Greenhouse Gas Control* 4 (2010): 638–646, https://doi.org/10.1016/j.ijggc.2009.12.013.

8. B. Q. Wang, X. Y. Wang, B. Wu, et al., "Organic Molecule Functionalization Enables Selective Electrochemical Reduction of Dilute CO_2 Feedstock," *Angewandte Chemie International Edition* 64 (2024): 202417196.

9. L. Y. Q. Xie, Y. M. Cai, Y. J. Jiang, et al., "Direct low concentration CO_2 electroreduction to multicarbon products via rate-determining step tuning," *Nature Communications* 15 (2024): 10386.

10. E. E. De Guzman, T.-H. Wang, M. A. B. Promentilla, and C.-Y. Lin, "Integrated Capture and Electroreduction of Low-Concentration CO_2 to CO Using Geopolymer|Graphene-Cobalt Phthalocyanine Composite," *Advanced Energy and Sustainability Research* 6 (2025): 2500080, https://doi.org/10.1002/aesr.202500080.

11. F. N. I. Sari, T.-H. Wang, M.-C. Hsieh, T.-H. Kuan, M. A. Camargo-Valero, and C.-Y. Lin, "Iodide-Mediated Electroreduction of Carbon Dioxide for Efficient and Selective Electrosynthesis of Multicarbon Products Over Copper Iodide Microcrystals," *Journal of Colloid and Interface Science* 696 (2025): 137847, https://doi.org/10.1016/j.jcis.2025.137847.

12. P. De Luna, C. Hahn, D. Higgins, S. A. Jaffer, T. F. Jaramillo, and E. H. Sargent, "What Would it Take for Renewably Powered Electrosynthesis to Displace Petrochemical Processes?," *Science* 364 (2019): aav3506, https://doi.org/10.1126/science.aav3506.

13. T.-H. Wang, C.-Y. Lin, Y.-C. Huang, and C.-Y. Li, "Facile Electrosynthesis of Polyaniline|Gold Nanoparticle Core-Shell Nanofiber for Efficient

Electrocatalytic CO_2 Reduction," *Electrochimica Acta* 437 (2023): 141500, https://doi.org/10.1016/j.electacta.2022.141500.

14. Y. M. Wang, F. Q. Yan, Q. Y. Wang, et al., "Single-Atom Tailored Atomically-Precise Nanoclusters for Enhanced Electrochemical Reduction of CO_2-to-CO Activity," *Nature Communications* 15 (2024): 1843, https://doi.org/10.1038/s41467-024-46098-x.

15. S. Ren, D. Joulié, D. Salvatore, et al., "Molecular Electrocatalysts can Mediate Fast, Selective CO_2 Reduction in a Flow Cell," *Science* 365 (2019): 367–369, https://doi.org/10.1126/science.aax4608.

16. J. W. Li, H. L. Zeng, X. Dong, et al., "Selective CO_2 Electrolysis to CO Using Isolated Antimony Alloyed Copper," *Nature Communications* 14 (2023): 340, https://doi.org/10.1038/s41467-023-35960-z.

17. S. B. Liu, C. Sun, J. Xiao, and J. L. Luo, "Unraveling Structure Sensitivity in CO_2 Electroreduction to Near-Unity CO on Silver Nanocubes," *ACS Catalysis* 10 (2020): 3158–3163, https://doi.org/10.1021/acscatal.9b03883.

18. T. Möller, W. Ju, A. Bagger, et al., "Efficient CO_2 to CO Electrolysis on Solid Ni–N–C Catalysts at Industrial Current Densities," *Energy & Environmental Science* 12 (2019): 640–647.

19. X. Zhang, Z. Wu, X. Zhang, et al., "Highly Selective and Active CO_2 Reduction Electrocatalysts Based on Cobalt Phthalocyanine/Carbon Nanotube Hybrid Structures," *Nature Communications* 8 (2017): 14675, https://doi.org/10.1038/ncomms14675.

20. X. M. Hu, M. H. Ronne, S. U. Pedersen, T. Skrydstrup, and K. Daasbjerg, "Enhanced Catalytic Activity of Cobalt Porphyrin in CO_2 Electroreduction upon Immobilization on Carbon Materials," *Angewandte Chemie International Edition* 56 (2017): 6468–6472, https://doi.org/10.1002/anie.201701104.

21. F. Lv, N. Han, Y. Qiu, X. Liu, J. Luo, and Y. Li, "Transition Metal Macrocycles for Heterogeneous Electrochemical CO_2 Reduction," *Coordination Chemistry Reviews* 422 (2020): 213435, https://doi.org/10.1016/j.ccr.2020.213435.

22. X. Zhang, Y. Wang, M. Gu, et al., "Molecular Engineering of Dispersed Nickel Phthalocyanines on Carbon Nanotubes for Selective CO_2 Reduction," *Nature Energy* 5 (2020): 684–692, https://doi.org/10.1038/s41560-020-0667-9.

23. G. Wang, S. Gong, M. Li, J. Liu, and X. Lv, "Efficient and Stable Metal Macrocyclic Molecular Catalyst for Electrocatalytic Reduction of CO_2 to CO," *Progress in Chemistry* 37 (2025): 173–184, https://doi.org/10.7536/PC240409.

24. W. S. Dean, T. L. Soucy, K. E. Rivera-Cruz, L. L. Filien, B. D. Terry, and C. C. L. McCrory, "Mitigating Cobalt Phthalocyanine Aggregation in Electrocatalyst Films Through Codeposition With an Axially Coordinating Polymer," *Small* 21 (2025): 2402293, https://doi.org/10.1002/smll.202402293.

25. M. Zhu, R. Ye, K. Jin, N. Lazouski, and K. Manthiram, "Elucidating the Reactivity and Mechanism of CO_2 Electroreduction at Highly Dispersed Cobalt Phthalocyanine," *ACS Energy Letters* 3 (2018): 1381–1386, https://doi.org/10.1021/acsenergylett.8b00519.

26. X. Wu, J. W. Sun, P. F. Liu, et al., "Molecularly Dispersed Cobalt Phthalocyanine Mediates Selective and Durable CO_2 Reduction in a Membrane Flow Cell," *Advanced Functional Materials* 32 (2022): 2107301, https://doi.org/10.1002/adfm.202107301.

27. Y. Wu, Z. Jiang, X. Lu, Y. Liang, and H. Wang, "Domino Electroreduction of CO_2 to Methanol on a Molecular Catalyst," *Nature* 575 (2019): 639–642, https://doi.org/10.1038/s41586-019-1760-8.

28. W. W. Kramer and C. C. L. McCrory, "Polymer Coordination Promotes Selective CO_2 Reduction by Cobalt Phthalocyanine," *Chemical Science* 7 (2016): 2506–2515, https://doi.org/10.1039/C5SC04015A.

29. N. Morlanes, K. Takanabe, and V. Rodionov, "Simultaneous Reduction of CO_2 and Splitting of H_2O by a Single Immobilized Cobalt Phthalocyanine Electrocatalyst," *ACS Catalysis* 6 (2016): 3092–3095.

30. Y. S. Wu, Z. Jiang, X. Lu, Y. Y. Liang, and H. L. Wang, "Domino Electroreduction of CO_2 to Methanol on a Molecular Catalyst," *Nature* 575 (2019): 639–642.

31. L. Zhu, Y.-X. Wang, L.-J. Chen, et al., "Single Molecular Dispersion of Crown Ether-Decorated Cobalt Phthalocyanine on Carbon Nanotubes for Robust CO_2 Reduction Through Host-Guest Interactions," *Angewandte Chemie International Edition* 64 (2025): 202418156, https://doi.org/10.1002/anie.202418156.

32. X. Zhang, Z. Wu, X. Zhang, et al., "Highly Selective and Active CO_2 Reduction Electrocatalysts Based on Cobalt Phthalocyanine/Carbon Nanotube Hybrid Structures," *Nature Communications* 8 (2017): 14675.

33. J. Su, J.-J. Zhang, J. Chen, et al., "Building a Stable Cationic Molecule/Electrode Interface for Highly Efficient and Durable CO_2 Reduction at an Industrially Relevant Current," *Energy & Environmental Science* 14 (2021): 483–492.

34. R. Wang, X. Wang, W. Weng, et al., "Proton/Electron Donors Enhancing Electrocatalytic Activity of Supported Conjugated Microporous Polymers for CO_2 Reduction," *Angewandte Chemie International Edition* 61 (2022): 202115503, https://doi.org/10.1002/anie.202115503.

35. J.-M. Chen, W.-J. Xie, Z.-W. Yang, and L.-N. He, "Cobalt Phthalocyanine Cross-Linked Polypyrrole for Efficient Electroreduction of Low Concentration CO2 To CO," *Chemsuschem* 15 (2022): 202201455.

36. J. Xiao, J. J. Masana, H. Dong, et al., "Mechanistic Understanding of 3d-Metal Phthalocyanine Catalysts: Heterostructure Regulation of d Z_2 Orbitals for Efficient CO_2 Reduction," *Journal of Materials Chemistry A* 11 (2023): 24359–24370, https://doi.org/10.1039/D3TA05834D.

37. Y. Yang, W. Zhang, G. Wu, et al., "Electronic Structure Tuning in Cu–Co Dual Single Atom Catalysts for Enhanced COOH* Spillover and Electrocalytic CO_2 Reduction Activity," *Angewandte Chemie International Edition* 64 (2025): 202504423, https://doi.org/10.1002/anie.202504423.

38. Y. Li, M. Yang, Z. Tian, et al., "Assembly of Copper Phthalocyanine on TiO_2 Nanorod Arrays as Co-catalyst for Enhanced Photoelectrochemical Water Splitting," *Frontiers in Chemistry* 7 (2019): 334, https://doi.org/10.3389/fchem.2019.00334.

39. T. Honda, T. Kojima, and S. Fukuzumi, "Proton-Coupled Electron-Transfer Reduction of Dioxygen Catalyzed by a Saddle-Distorted Cobalt Phthalocyanine," *Journal of the American Chemical Society* 134 (2012): 4196–4206, https://doi.org/10.1021/ja209978q.

40. V. Çakır, "Functional Chalcone-Substituted Tetrakis-Metallophthalocyanines: Synthesis and Spectroscopic Characterization," *Journal of Chemical Research* 44 (2020): 148–151.

41. D. Ledson and M. Twigg, "Acid-Base Behaviour of Phthalocyanine," *Inorganica Chimica Acta* 13 (1975): 43–46, https://doi.org/10.1016/S0020-1693(00)90175-0.

42. R. Seoudi, G. S. El-Bahy, and Z. A. El Sayed, "Ultraviolet and Visible Spectroscopic Studies of Phthalocyanine and Its Complexes Thin Films," *Optical Materials* 29 (2006): 304–312, https://doi.org/10.1016/j.optmat.2005.10.002.

43. Y. J. Zhang, L. S. Li, J. Jin, et al., "Organized Langmuir–Blodgett Monolayers and Multilayers Based on Semiamphiphilic Binuclear Phthalocyanine: Structural and Photovoltaic Characteristics," *Langmuir* 15 (1999): 2183–2187, https://doi.org/10.1021/la980466j.

44. K. Ishii and N. Kobayashi, in *The Porphyrin Handbook*, (Eds.: K. M. Kadish, K. M. Smith, R. Guilard). (Academic Press, 2003): 1–42.

45. X. Liang, Z. Chen, H. Wu, et al., "Enhanced NH_3 -Sensing Behavior of 2,9,16,23-Tetrakis(2,2,3,3-Tetrafluoropropoxy) Metal(II) Phthalocyanine/Multi-Walled Carbon Nanotube Hybrids: An Investigation of the Effects of Central Metals," *Carbon* 80 (2014): 268–278, https://doi.org/10.1016/j.carbon.2014.08.065.

46. Y. Xin, C. B. Musgrave, 3rd, J. Su, J. Li, et al., "Subtle Modifications in Interface Configurations of Iron/Cobalt Phthalocyanine-Based Electrocatalysts Determine Molecular CO_2 Reduction Activities," *Angewandte*

Chemie International Edition 64 (2025): e202420286, https://doi.org/10.1002/anie.202420286.

47. S. Gong, X. Han, W. Li, et al., "Paired Electrolysis for Efficient Coproduction of CO and S8 With Techno-Economic Analysis," *Chemical Engineering Journal* 507 (2025): 160286, https://doi.org/10.1016/j.cej.2025.160286.

48. W. Li, C. Yu, X. Song, et al., "Metal-Free Polyphthalocyanine With Implanted Built-In Electric Field Enabling High-Efficiency CO_2 Electroreduction," *Chemistry of Materials* 36 (2024): 1602–1611, https://doi.org/10.1021/acs.chemmater.3c02856.

49. J. Zhang, T. H. My Pham, Z. Gao, et al., "Electrochemical CO_2 Reduction Over Copper Phthalocyanine Derived Catalysts With Enhanced Selectivity for Multicarbon Products," *ACS Catalysis* 13 (2023): 9326–9335, https://doi.org/10.1021/acscatal.3c01439.

50. Y.-L. Yang, Q. Li, P. Liu, et al., "Subtle Tuning of Catalytic Well Effect in Phthalocyanine Covalent Organic Frameworks for Selective CO_2 Electroreduction Into C_2H_4," *Advanced Materials* 37 (2025): 2415799, https://doi.org/10.1002/adma.202415799.

51. Z. Weng, Y. Wu, M. Wang, et al., "Active Sites of Copper-Complex Catalytic Materials for Electrochemical Carbon Dioxide Reduction," *Nature Communications* 9 (2018): 415, https://doi.org/10.1038/s41467-018-02819-7.

52. E. Boutin, A. Salamé, and M. Robert, "Confined Molecular Catalysts Provide an Alternative Interpretation to the Electrochemically Reversible Demetallation of Copper Complexes," *Nature Communications* 13 (2022): 4190, https://doi.org/10.1038/s41467-022-31661-1.

53. Q. Wan, Y. Liu, C. Ke, et al., "Insight on Performance Degradation of Phthalocyanine Cobalt-Based Gas Diffusion Cathode for Carbon Dioxide Electrochemical Reduction," *ACS Sustainable Chemistry & Engineering* 9 (2021): 17214–17220, https://doi.org/10.1021/acssuschemeng.1c07158.

54. C. Yang, Z. Gao, D. Wang, et al., "Bimetallic Phthalocyanine Heterostructure Used for Highly Selective Electrocatalytic CO_2 Reduction," *Science China Materials* 65 (2022): 155–162, https://doi.org/10.1007/s40843-021-1749-5.

55. A. Ghatak, G. S. Shanker, Y. Pearlmutter, A. Fryder, R. Shimoni, and I. Hod, "Dual Molecular Catalyst-Based Tandem That Enables Electrocatalytic CO_2 −Formaldehyde−Methanol Cascade Conversion," *Journal of the American Chemical Society* 147 (2025): 20329–20337, https://doi.org/10.1021/jacs.5c00316.

56. Z. Zhang, J. Sun, F. Wang, and L. Dai, "Efficient Oxygen Reduction Reaction (ORR) Catalysts Based on Single Iron Atoms Dispersed on a Hierarchically Structured Porous Carbon Framework," *Angewandte Chemie International Edition* 57 (2018): 9038–9043, https://doi.org/10.1002/anie.201804958.

57. Z. Zhang, M. Dou, J. Ji, and F. Wang, "Phthalocyanine Tethered Iron Phthalocyanine on Graphitized Carbon Black as Superior Electrocatalyst for Oxygen Reduction Reaction," *Nano Energy* 34 (2017): 338–343, https://doi.org/10.1016/j.nanoen.2017.02.042.

58. A. J. Medford, A. Vojvodic, J. S. Hummelshøj, et al., "From the Sabatier Principle to a Predictive Theory of Transition-Metal Heterogeneous Catalysis," *Journal of Catalysis* 328 (2015): 36–42, https://doi.org/10.1016/j.jcat.2014.12.033.

59. S. Jiao, X. Fu, and H. Huang, "Descriptors for the Evaluation of Electrocatalytic Reactions: D-Band Theory and Beyond," *Advanced Functional Materials* 32 (2022): 2107651, https://doi.org/10.1002/adfm.202107651.

60. X. Zhang, Y. Wang, M. Gu, et al., "Molecular Engineering of Dispersed Nickel Phthalocyanines on Carbon Nanotubes for Selective CO_2 Reduction," *Nature Energy* 5 (2020): 684–692.

61. Y. Shi, Y. Wang, C.-L. Dong, et al., "Localized Geometry Determined Selectivity of Iodide-Derived Copper for Electrochemical CO_2 Reduction," *Advanced Energy Materials* 13 (2023): 2203896, https://doi.org/10.1002/aenm.202203896.

62. S.-C. Huang, H.-C. Yu, C.-K. Peng, Y.-G. Lin, and C.-Y. Lin, "P-Doped NiFe Alloy-Based Oxygen Evolution Electrocatalyst for Efficient and Stable Seawater Splitting and Organic Electrosynthesis at Neutral pH," *Small* 21 (2025): 2408957, https://doi.org/10.1002/smll.202408957.

63. S. J. Clark, M. D. Segall, C. J. Pickard, et al., "First Principles Methods Using CASTEP," *Zeitschrift für Kristallographie - Crystalline Materials* 220 (2005): 567–570.

64. C. Motta, F. El-Mellouhi, S. Kais, N. Tabet, F. Alharbi, and S. Sanvito, "Revealing the Role of Organic Cations in Hybrid Halide Perovskite $CH_3NH_3PbI_3$," *Nature Communications* 6 (2015): 7026, https://doi.org/10.1038/ncomms8026.

65. A. Tkatchenko and M. Scheffler, "Accurate Molecular Van Der Waals Interactions From Ground-State Electron Density and Free-Atom Reference Data," *Physical Review Letters* 102 (2009): 073005, https://doi.org/10.1103/PhysRevLett.102.073005.

66. J. P. Perdew, J. A. Chevary, S. H. Vosko, et al., "Atoms, Molecules, Solids, and Surfaces: Applications of the Generalized Gradient Approximation for Exchange and Correlation," *Physical Review B* 46 (1992): 6671–6687.

67. J. P. Perdew, K. Burke, and M. Ernzerhof, "Generalized Gradient Approximation Made Simple," *Physical Review Letters* 77 (1996): 3865–3868.

68. D. Vanderbilt, "Soft Self-Consistent Pseudopotentials in a Generalized Eigenvalue Formalism," *Physical Review Letters* 41 (1990): 7892.

Supporting Information

Additional supporting information can be found online in the Supporting Information section.

Supporting File: smll72639-sup-0001-SuppMat.docx.